**Climate
of the Past
Discussions**

Robustness of the Atlantic-Pacific flow reversal in the early miocene

E. Bernsen and H. A. Dijkstra

Institute for Marine and Atmospheric research Utrecht, Utrecht University,
Utrecht, The Netherlands

Correspondence to: H. A. Dijkstra (h.a.dijkstra@uu.nl)

E. Bernsen and
H. A. Dijkstra

Abstract

Based on modeling results and interpretations of observations, it has been suggested that during the early Miocene, a reversal of the Atlantic-Pacific ocean flow through the Panama Strait has occurred. During the Oligocene the net transport was westward, from the Atlantic into the Pacific, whereas in the Miocene the sign of this transport likely reversed to a net eastward transport into the Atlantic. With a global ocean model for the Oligocene and Miocene continental configurations we study the robustness of this flow reversal by carrying out a broad sensitivity analysis, including bottom topography, details of the continental geometry and surface forcing. This sensitivity study is efficiently done by using recent methodology to compute equilibrium solutions to the model. The Atlantic-Pacific flow reversal appears a very robust feature of the global ocean model.

1 Introduction

Due to tectonic plate movements the continental geometry in paleo epochs was completely different from present-day geometry, resulting in completely different global ocean circulation patterns. The opening and closing of gateways, in particular, may have had substantial influence on both the global surface circulation and the meridional overturning. In this paper, we concentrate on ocean circulation changes during the period between the Oligocene (34–23 My) and Miocene (23–5 My).

In the early Oligocene the Tasmanian Gateway and Drake Passage were only very narrow, preventing the existence of a strong Antarctic Circumpolar Current (ACC). Due to tectonic plate movements, South America and Australia moved northward, widening these two gateways (Barker and Burrell, 1977; Exon et al., 2001) and allowing a stronger ACC to develop in the Miocene. Another change occurred in the Thetys Seaway, which provided a direct connection between the North Atlantic and the Indian Ocean in the Oligocene. There likely was a westerly (Hallam, 1969)

current passing from the Indian Ocean through the Thetys Seaway to the Atlantic Ocean and then through Panama Strait and the Pacific back to the Indian Ocean, a so-called circum-equatorial current. During the transition from the Oligocene to the Miocene the Thetys Seaway first shallowed and finally was closed off completely (Ricou, 1987; Dercourt et al., 2000).

Using a shallow-water model of the wind-driven ocean circulation for many different continental geometries in the Cenozoic, the strengthening of the ACC and the disappearance of the circum-equatorial current were found within the Oligocene-Miocene period in Omta and Dijkstra (2003). As a consequence of these changes in gateways, however, they also found a flow reversal through the Panama Strait, which (in the model) occurs in the early Miocene. The physical mechanism of this flow reversal was explained by combining the linear island rule (Godfrey, 1989) with the continuity equation to arrive at a diagnostic relation between the Panama Strait transport and that through the Thetys Seaway and through the Drake Passage. According to this relation, the widening of Drake Passage and the corresponding increase in the strength of the ACC and the closing of the Thetys Seaway both have the effect to increase the eastward transport through the Panama Strait, eventually leading to a reversal of the sign of this transport.

In von der Heydt and Dijkstra (2005), the mechanism suggested in Omta and Dijkstra (2003) is shown to apply in the much more realistic setting of a fully coupled climate model, an earlier version of the CCSM (version 1.4). They performed simulations for both the Oligocene and Miocene and found that the diagnostic relation, as proposed in Omta and Dijkstra (2003), is satisfied quite well. The predicted transport through Panama Strait is 9% larger and 20% smaller than the actual transport for the Oligocene and Miocene simulations, respectively. Because of this good agreement, they conclude that the flow reversal is mainly caused by the wind-driven ocean circulation, which in turn strongly depends on the continental configuration.

Only circumstantial geological evidence to support the Atlantic-Pacific flow reversal is found for example by the disappearance of corals in the Caribbean Sea (Nesbitt and Young, 1997; Budd et al., 1994; Edinger and Risk, 1995). It appears that many corals in the Caribbean Sea, especially the ones not resistant to cold waters, suddenly disappeared in the early Miocene. Since a flow reversal in Panama Strait would allow cold water from the Pacific to enter the Caribbean, this provides a likely explanation for the disappearance of these corals (von der Heydt and Dijkstra, 2005).

The model used in Omta and Dijkstra (2003) is relatively simple and may miss important physical processes relevant for this reversal, such as effects of baroclinic pressure gradients. In von der Heydt and Dijkstra (2005) only results of two model simulations are presented and a flat bottom was used, such that the gateway representation may be unrealistic. In this paper, we therefore undertake an extensive sensitivity study on this flow reversal with a global ocean model, the Modular Ocean Model (MOM) version 4.0. We are able to do so efficiently using recently developed methods based on Jacobian Free Newton Krylov (JFNK) techniques to compute equilibrium solutions of MOM4 (Bernsen et al., 2009).

Details of the model and the numerical methods used are given in Sect. 2. Here we also present our equilibrium solutions for the reference configurations for the Miocene and Oligocene geometries and a comparison between the efficiency of the JFNK method and classical time stepping is made. The reference solutions are the starting point for the sensitivity analysis in Sect. 3. We investigate the sensitivity of the transport through Panama Strait with respect to changes in bottom topography, continental geometry and forcing. In Sect. 4 the results are summarized and discussed.

2 Formulation

In Sect. 2.1, the ocean model used and the particular continental configurations and forcing are described. This is followed by a short description of the application of the JFNK methodology in Sect. 2.2.

Robustness of the Atlantic-Pacific flow reversal

E. Bernsen and
H. A. Dijkstra

Title Page

Abstract | Introduction

Conclusions | References

Tables | Figures

|◄ | ►|

◄ | ►

Back | Close

Full Screen / Esc

Printer-friendly Version

Interactive Discussion

2.1 Model configuration

In this study we used the global version of the Modular Ocean Model version 4 (MOM4) which is described in detail in Griffies et al. (2004). MOM4 is a primitive equation model that solves the hydrostatic momentum equations, the continuity equation and the equations for temperature and salinity on a so-called Arakawa B-grid. In addition, a free-surface formulation is applied where the sea-surface height is part of the solution. In the version we use, horizontal friction is parametrized with a Laplacian operator with a constant eddy-viscosity coefficient of $A_H = 2.5 \times 10^5 \, \text{m}^2 \, \text{s}^{-1}$ and in the vertical direction a constant eddy-viscosity coefficient of $A_V = 10^{-3} \, \text{m}^2 \, \text{s}^{-1}$.

The geometries for the Miocene and Oligocene simulations are based on reconstructions from the Ocean Drilling Stratigraphic Network (ODSN) and are the same as used in von der Heydt and Dijkstra (2005). Our reference bottom topography is a flat bottom just as in von der Heydt and Dijkstra (2005), with a depth of $D_0 = 5000 \, \text{m}$. The zonal resolution in MOM4 is 3.6° while the latitudinal resolution ranges between 0.9° and 1.8°. This is similar to that in von der Heydt and Dijkstra (2005), except that we use a tripolar grid (Murray, 1996) to avoid a singularity at the North pole. Above 60° N the grid is deformed such that two poles are located at the Eurasian and North American continents. In the vertical we use 14 layers, ranging from a thickness of 25 m near the surface towards 950 m for the deep ocean.

The surface wind fields to drive the ocean flow were obtained from the time mean (over the last 20 year) of the equilibrium solutions for the Miocene and Oligocene configurations in von der Heydt and Dijkstra (2005). Because the flow reversal is mainly a wind-driven phenomenon, temperature and salinity are not treated as dynamic variables, but have prescribed fixed values as determined from the equilibrium solutions of von der Heydt and Dijkstra (2005). This results in a density field and the resulting baroclinic pressure gradients (i.e. pressure gradients due to density differences) that act as a forcing on the momentum equations. To compute the density field a linear

Title Page

Abstract | Introduction

Conclusions | References

Tables | Figures

◄ | ►►

◄ | ►

Back | Close

Full Screen / Esc

Printer-friendly Version

Interactive Discussion

equation of state was used

$$\rho = \rho_0 - \alpha_0(T - T_0) + \beta_0(S - S_0) \tag{1}$$

with $\alpha_0 = 10^{-1}\,\mathrm{kg\,m^{-3}\,K^{-1}}$ the thermal expansion coefficient, $\beta_0 = 7.6 \times 10^{-1}\,\mathrm{kg\,m^{-3}\,psu^{-1}}$ the saline contraction coefficient and $\rho_0 = 1035\,\mathrm{kg\,m^{-3}}$, $T_0 = 12.5°\mathrm{C}$,

5 $S_0 = 35\,\mathrm{psu}$ a reference density, temperature and salinity, respectively. Note that this is a significant simplification compared the full CCSM model used in von der Heydt and Dijkstra (2005). Compared to the shallow-water model used in Omta and Dijkstra (2003), MOM4 adds vertical structure and the presence of full stratification to the flow.

The prescribed wind-stress field $\boldsymbol{\tau}_0 = (\tau_{0,\phi}, \tau_{0,\theta})$, with $\tau_{0,\phi}$ and $\tau_{0,\theta}$ the zonal and

10 meridional components, for the Oligocene and Miocene is plotted in Fig. 1a and b, respectively. The wind-stress field is generally largest on the east coast of continents with maximum values of approximately 0.58 Pa for the Oligocene and 0.66 Pa for the Miocene. For both epochs the spatially averaged wind-stress strength is approximately 0.07 Pa. The basic pattern of wind-stress field is similar for both epochs and qualita-

15 tively not very different from the present-day wind-stress field. In Fig. 1c and d the sea surface temperature (SST) fields are plotted for the Oligocene and Miocene, respectively. Globally averaged SST is for both configurations approximately 21°C, ranging from 33°C in the tropics to −2°C near Antarctica and in the Arctic seas. In both configurations the SST in the Pacific is highest in the western Pacific and on average

20 slightly higher in the Pacific than in the Atlantic. However, when considering the depth-averaged temperature field (not shown here) the Atlantic is clearly warmer than the Pacific. In Fig. 1e and f, the sea surface salinity (SSS) for both epochs is plotted. Like in the present-day situation, salinity in the Atlantic is much higher than in the Pacific. In the Miocene (Fig. 1f) the Thetys Sea is closed off resulting in a higher salinity in the

25 Mediterranean, since supply of fresh water from the Indian Ocean is no longer available. In the Atlantic, however, the surface salinity is in general higher in the Oligocene (Fig. 1e) than in the Miocene.

Title Page

Abstract | Introduction

Conclusions | References

Tables | Figures

|◄ | ►|

◄ | ►

Back | Close

Full Screen / Esc

Printer-friendly Version

Interactive Discussion

2.2 Numerical methods

To efficiently compute equilibrium solutions for different continental configurations and and parameters of the model, we use the Jacobian-Free Newton-Krylov (JFNK) methodology of Bernsen et al. (2009). As we are interested in finding equilibrium solutions, we solve the steady state equations in MOM4 which can be written as

$$F(x) = 0. \tag{2}$$

where x is the state vector consisting of all dependent variables at all grid points. In the JFNK method this system of non-linear equations is solved using a Newton-Raphson iteration. Starting from an initial guess x_0, the iteration is given by

$$x_{k+1} = x_k + \Delta x_{k+1} \tag{3}$$

with Δx_{k+1} satisfying

$$J(x_k)\, \Delta x_{k+1} = -F(x_k), \tag{4}$$

where J is the Jacobian matrix of $F(x_k)$ defined by $J_{ij} = \partial F_i / \partial x_j$. Krylov methods, here FGMRES (Saad, 1996), are now used to solve the linear systems Eq. (4). In a Jacobian-Free method, a finite difference approximation for the matrix-vector product is applied, exploiting the fact that Krylov methods only require the effect of applying J to a vector. A one-sided finite difference approximation

$$J(x_k)v \approx \frac{F(x_k + \epsilon v) - F(x_k)}{\epsilon} \tag{5}$$

is used here, with ϵ a small parameter. The advantage of this approach is that now only the residual F is required and given an explicit time stepping code such as MOM4, this is much easier to obtain than an explicit representation of the full Jacobian J.

The set-up of the JFNK method used here is almost the same as that in Sect. 3.3 of Bernsen et al. (2009). The only difference is in the (outer) FGMRES method that is used to solve the linear systems arising from Newton's method (see Eq. (7)

in Bernsen et al., 2009). The FGMRES iteration is stopped when a solution Δx_{k+1} is found, that satisfies

$$\|\mathbf{J}(x_k)\Delta x_{k+1} + F(x_k)\|_2 < \epsilon \|F(x_k)\|_2. \tag{6}$$

In Bernsen et al. (2009) we used a value of $\epsilon = 10^{-3}$, but here we use a larger value
5 $\epsilon = 10^{-2}$. Further, the maximum number of FGMRES iterations is increased to 100 (instead of 50 in Bernsen et al., 2009).

   Using these settings the JFNK method converges and in Table 1 the convergence properties are shown for the Oligocene configuration as in Fig. 1. Starting from the fourth Newton step the residual improves with a factor of 10^{-2}, in agreement with the
10 stopping criterion used for the FGMRES iteration. Further we note that the total number of Newton iterations and the number of FGMRES iterations per Newton step is significantly higher than for the idealized examples in Sect. 3.3 of Bernsen et al. (2009). The increase in the number of Newton iterations can be explained by the fact that here a less stringent stopping criterion for FGMRES was used. The number of un-
15 knowns for the linear systems here is with a value of $N \approx 210\,000$ much larger than that for the highest resolution ($N \approx 130\,000$) tested in Sect. 3.3 of Bernsen et al. (2009). Also here a complicated geometry is used rather than the idealized setup as in Bernsen et al. (2009). This possibly explains the increase of the number of FGMRES iterations per Newton step.

20   To verify the correctness of the result of the JFNK method we compared an equilibrium solution with this method with one obtained by just running MOM4 forward in time. In this simulation we start from a state of rest and zero surface-elevation, and integrate forward in time using a baroclinic time step of 0.25 day and 100 barotropic sub-steps per baroclinic step. In Fig. 2 we plot the maximum difference between the barotropic
25 streamfunction obtained using the JFNK method and that obtained using time stepping as a function of the length of the spin-up run. The difference approaches zero for both Oligocene and Miocene configurations and hence the JFNK method finds the same equilibrium as the MOM4 in time stepping mode. Note that the spin-up time-scale is relatively short here, because temperature and salinity are not dynamic variables.

Robustness of the Atlantic-Pacific flow reversal

E. Bernsen and
H. A. Dijkstra

In Table 2 we list the CPU time used by the JFNK method and the time used by a spin-up run of five year using the time stepper. The JFNK method achieves a speed-up of approximately a factor of 4.5 in comparison with the five year spin-up run for both model configurations. Of course the accuracy of the time stepper depends on the length of the spin-up run. A time stepping spin-up run of one year would take approximately as much time as the JFNK method. Hence, to obtain accurate solutions the JFNK method is significantly faster than the time stepping run.

The barotropic streamfunction of the equilibrium global ocean circulation in MOM4 for the Oligocene Fig. 3a and Miocene Fig. 3b are qualitatively similar to Fig. 7 in von der Heydt and Dijkstra (2005). In the south we clearly see the presence of the Antarctic Circumpolar Current (ACC) in the Miocene and Oligocene. In the Oligocene the ACC has a strength of approximately 80 Sv whereas in the Miocene this has increased to approximately 120 Sv. Due to the flat bottom topography the ACC strength is likely overestimated, but still the value 120 Sv in the Miocene is slightly lower than the present day value of approximately 125 Sv. Western boundary currents are formed by the poleward flowing parts of the subtropical gyres. The gyre just above the equator in the Pacific basin increases in strength during the transition from Oligocene to Miocene. Just below the equator a gyre extends from the Indian basin into the Pacific basin due to the absence of the Indonesian through flow.

3 Results

In Sect. 1 it was already mentioned that in earlier studies (Omta and Dijkstra, 2003) the net flow in Panama Strait changed from a westward direction to an eastward direction during the transition from the Oligocene to the Miocene. In this section, the robustness of this flow reversal will be studied using the MOM4 solutions.

E. Bernsen and H. A. Dijkstra

Title Page

Abstract | Introduction

Conclusions | References

Tables | Figures

◄ | ►

Back | Close

Full Screen / Esc

Printer-friendly Version

Interactive Discussion

3.1 Flow reversal

To investigate the flow reversal for the equilibrium solutions determined in the previous section, we compute the transports Φ_D, Φ_P, Φ_T, Φ_{SA} and Φ_A as the transport through Drake Passage, Panama Strait, Thetys Sea, the transport through the gateway between the tip of South Africa and Antarctica and the transport from the North Atlantic polewards into the Arctic seas, respectively (see Fig. 4). All transports are defined to have a positive sign for a transport into the Atlantic.

In Table 3 all these transports are listed for the reference cases. In the Miocene the transport Φ_T vanishes because the Thetys Seaway is closed and in the Oligocene the transport Φ_A is negligible because the seaway from the North Atlantic into the Arctic regions is almost blocked. More interesting is that the flow through Panama Strait is westwards for the Oligocene but eastwards in the Miocene, confirming that the reversal of the flow, as found in the studies of Omta and Dijkstra (2003) and von der Heydt and Dijkstra (2005), is also present in our model configuration.

For the equilibrium solutions one would expect the total transport $\Phi_{tot} = \Phi_D + \Phi_{SA} + \Phi_P + \Phi_T + \Phi_A$ to vanish. Indeed, in the last row of Table 3, the total transport is negligible compared to the other transports. The total transport does not vanish completely and this is due to the smoothing that is applied to the surface height equation in MOM4. In Sect. 2.2 of Bernsen et al. (2009) we already noted that this smoothing is applied to avoid a null-mode on the B-grid and the equation for surface height becomes

$$\frac{\partial \eta}{\partial t} + \nabla \cdot \boldsymbol{U} = \nabla \cdot (K_H \nabla \eta) \tag{7}$$

with η the surface elevation, $\boldsymbol{U}$ the depth-integrated horizontal velocity and K_H the smoothing coefficient. Using Eq. (7), Gauss' Theorem and the fact that we reached an equilibrium solution ($\partial \eta / \partial t = 0$), we can write for the total transport

$$\Phi_{tot} = \oint_{\partial A} \boldsymbol{U} \cdot \mathrm{d}\hat{n} = -\int_A \nabla \cdot \boldsymbol{U} \mathrm{d}A = \int_A \frac{\partial \eta}{\partial t} \mathrm{d}A - \int_A \nabla \cdot (K_H \nabla \eta) \mathrm{d}A = \oint_{\partial A} K_H \nabla \eta \cdot \mathrm{d}\hat{n} \tag{8}$$

E. Bernsen and
H. A. Dijkstra

where A is the region of the Atlantic basin, ∂A is the boundary of A and $\hat{n}$ the unit vector into the Atlantic basin. Hence, for $K_H \neq 0$ we generally have that $\Phi_{tot} \neq 0$ and performing additional Newton steps (or a longer spin-up run) will not result in smaller values of the total transport Φ_{tot}. Furthermore, in Fig. 2 we see that the error in the barotropic streamfunction after five years of time integration is of the same order as the error in the total transport, indicating that further time integration does not add any accuracy in the transport.

3.2 A simple model for the Atlantic-Pacific transport

In Omta and Dijkstra (2003) a linear relation was proposed to predict the transport through Panama Strait from the transport in the Thetys Seaway and Drake Passage. We slightly generalize this model here because of the presence of the transport Φ_A which was absent in Omta and Dijkstra (2003).

The continuity equation provides us with two constraints given by

$$\Phi_P + \Phi_T + \Phi_A = \Phi_S \tag{9}$$

$$\Phi_D + \Phi_{SA} + \Phi_S = 0 \tag{10}$$

with Φ_S the transport between the North and South Atlantic, a positive value meaning a transport from the North Atlantic into the South Atlantic. In Omta and Dijkstra (2003) the linear island rule (Godfrey, 1989) is approximated using the following expression

$$f_D \Phi_D + f_S \Phi_S + f_{SA} \Phi_{SA} = \rho_0^{-1} \oint_C \boldsymbol{\tau}_0 \cdot d\hat{s} \tag{11}$$

with ρ_0 a reference density, $\boldsymbol{\tau}_0$ the wind-stress. C is the closed contour starting at the tip of South Africa towards Antarctica, following the Antarctic coastline westward up to Drake Passage, then northward across Drake Passage towards the southern tip of South America. It then follows the western coastline of South America toward the northern tip of South America, crossing the Atlantic towards the west coast of Africa

and finally following this coastline southward to its starting point in South Africa (see Fig. 4). Furthermore, the vector $\hat{s}$ is the unit vector directed tangent to the contour C and f_D, f_{SA} and f_S are representative values of the Coriolis parameter corresponding to the location of the transports Φ_D, Φ_{SA} and Φ_S, respectively. Note that equation Eq. (4)

5 is obtained from vertically integrating the momentum equations followed by a contour integral over C. In deriving Eq. (4), friction, inertial and bottom topography terms are neglected

From the equations (Eqs. 9, 10 and 4) we can eliminate the variables Φ_{SA} and Φ_S to arrive at the linear equation

$$10 \quad \Phi_P = -\Phi_T - \Phi_A + \delta\Phi_D + \delta_\tau \tag{12}$$

with

$$\delta = \frac{f_{SA} - f_D}{f_S - f_{SA}} \tag{13}$$

and

$$\delta_\tau = \rho_0^{-1} \frac{\oint_C \boldsymbol{\tau}_0 \cdot \mathrm{d}\hat{s}}{f_{SA} - f_S}. \tag{14}$$

15 In Table 3 we see that for our equilibrium solutions the transport Φ_A is relatively small and for $\Phi_A = 0$, the relation above reduces to that in Omta and Dijkstra (2003).

Values of δ_τ were estimated in von der Heydt and Dijkstra (2005) from the wind stress field along the contour and as we use the same forcing and geometry, we use their values as being representative. For the value of δ, we use the average value of the Corio-

20 lis parameter over the part of the closed contour C corresponding to the transports Φ_D, Φ_{SA} and Φ_S, respectively, similar as in von der Heydt and Dijkstra (2005). This results in a value of $\delta_\tau = 2.4$ Sv and $\delta = 9.551 \times 10^{-2}$ for the Oligocene and $\delta = 9.345 \times 10^{-2}$ and $\delta_\tau = 1.4$ Sv for the Miocene. With the values for Φ_A, Φ_D and Φ_T from Table 3, we find $\Phi_P = -3.85$ Sv for the Oligocene and $\Phi_P = 12.83$ Sv for the Miocene. Consid-

25 ering all the approximations made, this is nice result, as it shows that this diagnostic

model for Φ_P also indicates a flow reversal. In the following sections we will refer to the transport diagnosed through Eq. (12) as the "predicted" transport.

3.3 Bottom topography

As mentioned in Sect. 1, the closing of the Thetys Seaway and opening of Drake Passage are the main reasons for the flow reversal to occur. We now model these changes in more detail, by putting a ridge first in the Thetys Seaway and next in the Drake Passage for the Oligocene geometry and compute equilibrium solutions for several values of the height of the ridge.

The ridges are modelled using the following shape of the bottom topography

$$D(\phi,\theta) = D_0 - \max(0, H - \gamma d(\phi,\theta)) \tag{15}$$

with $D(\phi,\theta)$ the depth of the ocean, $D_0 = 5000\,\text{m}$ the reference depth, H the maximum height of the ridge, $\gamma = 4 \times 10^{-3}$ the slope of the ridge and $d(\phi,\theta)$ the spherical distance from the point (ϕ,θ) to the section over which the transport Φ_T (or Φ_D) is calculated. This section is defined by the shortest path over the sphere between two points A and B with spherical coordinates (ϕ_A,θ_A) and (ϕ_B,θ_B), respectively (see Table 4).

For the Thetys as well as the Drake Passage case, we now create ten bottom topographies with ridges varying in height from $H = 0$ to $H = 4500\,\text{m}$. In Fig. 5a and b we show the bottom topography for a ridge of maximum height $H = 4500\,\text{m}$ in the Thetys Seaway and Drake Passage, respectively. Note that for the ridge in Drake Passage, the bottom topography is modified along the boundary of the South American continent up to a latitude of approximately 30°S and this is due to the relatively low latitude of the point B, one of the points that determines the section over which the transport Φ_D is calculated (see Table 4).

To compute the equilibrium solutions corresponding to the bathymetries we would ideally like to use a continuation method like in Bernsen et al. (2009). However, when the height of the ridge is increased the number of grid points in the vertical direction reduces, affecting the size of the state vector. This makes applying a continuation

method difficult. Therefore, for each value of H we apply a new spin-up using JFNK as described in Sect. 2.2.

In Fig. 6a the transports Φ_P, Φ_D, Φ_{SA}, Φ_T and Φ_A are plotted as a function of the height H of the ridge in the Thetys Seaway, with a detail in Fig. 6b. The transports Φ_D, Φ_{SA} and Φ_A change only very little, none of them changing more than 0.01 Sv. The transports through Panama Strait and the Thetys Seaway show large changes. As the ridge becomes higher the westward transport Φ_T and $-\Phi_P$ through the Thetys Seaway and Panama Strait both reduce and for $H > 3500$ m the flow in Panama Strait reverses from a westward to eastward direction. Even if a complete closing of the Thetys Seaway in the early Miocene did not happen (Dercourt et al., 2000), this would not have prevented the flow reversal in Panama Strait from occurring. In Fig. 6c we plot the difference in barotropic streamfunction $\Delta\Psi_B = \Psi_B - \Psi_{B,0}$ with $\Psi_{B,0}$ the streamfunction in the reference configuration. We clearly see that the main changes in the global flow pattern occur in the circumequatorial current, consistent with the results in Fig. 6a.

Since in our configurations only bottom topography is adjusted and wind-stress remains constant, it follows from Eq. (12) that the change in the transport through Panama Strait is approximated by

$$\Delta\Phi_P = -\Delta\Phi_T - \Delta\Phi_A + \delta\Delta\Phi_D. \tag{16}$$

Here $\Delta\Phi_P = \Phi_P - \Phi_{P,0}$, $\Delta\Phi_T = \Phi_T - \Phi_{T,0}$, $\Delta\Phi_A = \Phi_A - \Phi_{A,0}$ and $\Delta\Phi_D = \Phi_D - \Phi_{D,0}$ with $\Phi_{P,0}$, $\Phi_{T,0}$, $\Phi_{A,0}$ and $\Phi_{D,0}$ the transports for the reference configuration with a flat bottom. In Fig. 6d we then compare the actual change in transport through Panama Strait to the prediction according to Eq. (16). Note that the lines for actual and predicted transport overlap and the maximum error in the prediction is as little as 3.3×10^{-3} Sv. Because of the very small changes in Φ_D the actual value of δ is not very important in this case.

For the ridge in Drake Passage, we also determine the equilibrium solutions using the JFNK method and the transports Φ_P, Φ_D, Φ_{SA}, Φ_T and Φ_A are plotted as a function of the ridge height H in Fig. 7a (detail in Fig. 7b). Now, increasing the ridge has

E. Bernsen and
H. A. Dijkstra

the effect that the ACC is strongly reduced as indicated by the decrease in Φ_D and $-\Phi_{SA}$. A relatively low ridge of $H < 1000$ m has a relatively large impact, whereas the additional decrease in the ACC for ridges 1000 m $< H < 3500$ m is relatively small. For a maximum ridge height $H = 4500$ m the strength of the ACC is reduced with 55 Sv to a value of approximately 24 Sv. In Fig. 7b we see that changes in transport through the Thetys Sea way and Panama Strait are much smaller. For the maximum ridge height of $H = 4500$ m these changes are only 0.65 Sv for the Thetys Seaway and 1.06 Sv for Panama Strait. In Fig. 7c the difference in barotropic streamfunction $\Delta\Psi_B$ with respect to the reference configuration of Sect. 2.1 is plotted. This shows that indeed the main changes in the flow occur in the region of the ACC, whereas other regions are relatively unaffected.

In Fig. 7d we plot the actual change in transport through Panama Strait $\Delta\Phi_P$ and the predicted transport change according to Eq. (16). With a maximum error of 3.55 Sv, here the correspondence between the diagnosed and actual value is not nearly as good as in the case with a ridge in the Thetys Seaway, that we have seen earlier. Apparently neglecting inertial, friction and bottom topography, required for deriving Eq. (16), is not allowed in this situation. When comparing Fig. 7a and d we clearly see that the behavior of the transport Φ_D is reflected in the transport change $\Delta\Phi_P$ according to Eq. (16). For ridge heights 1000 m $< H < 3500$ m, Φ_D and $\Delta\Phi_D$ both remain relatively constant. Using different representative values of f_D, f_{SA} and f_S can certainly improve the results of the island rule. However, from the shapes of actual and predicted transport change $\Delta\Phi_P$ in Fig. 7d we can already see, that even for an optimal value of δ the change in transport through Panama Strait, according to Eq. (16), will not be very accurate. Although the prediction itself is not very good, we observe that at least the sign of actual and predicted transport change is the same. Both indicate that a decrease in ACC strength results in an increase in the westward transport through Panama Strait.

3.4 Continental geometry

In this section we consider changes in the continental geometry rather than bottom to-pography. Omta and Dijkstra (2003) made the interesting remark that the flow reversal depends on the fact that the tip of South Africa is located at a lower latitude than Drake Passage. Indeed, if South Africa would be at a higher latitude than Drake Passage, then $f_D > f_{SA}$ and hence $\delta < 0$. In that case a strengthening of the ACC would increase the westward transport in Panama Strait, possibly preventing the flow reversal from occurring.

To test this, we consider the Miocene geometry and extend the tip of South Africa southward by adding land-cells between $16.2°$ E $< \phi < 30.6°$ E. In addition to the reference geometry we create ten new geometries with the tip of South Africa extended southwards by 1–10 grid points. Each of these geometries has a flat bottom topography, just like the reference configuration. For the geometry where South Africa is maximally extended southward, the latitude of the tip of South Africa and Drake Passage are equal and the bathymetry for this case is plotted in Fig. 8a.

For each geometry we perform a spin-up simulation using the JFNK method as described in Sect. 2.2. Note that since only land cells are added and not ocean cells, interpolating the prescribed temperature and salinity to the new geometries poses no problems at all. In Fig. 8b the transports Φ_D, Φ_{SA}, Φ_A and Φ_P are plotted as a function of θ_{SA}. When South Africa is extended southwards, we see a decrease in Φ_D and $-\Phi_{SA}$, representing a decrease in the strength of the ACC. When θ_{SA} approaches the latitude of Drake Passage the decrease in ACC strength accelerates. More interestingly, as θ_{SA} decreases, we find that the eastward flow through Panama Strait decreases. When $\theta_{SA} = 58.0°$ S and $\delta = -1.1 \times 10^{-2}$ the flow in Panama Strait turns from eastward into westward. Hence, for a geometry with this latitude θ_{SA} the flow would remain westward during the Oligocene to Miocene transition and no flow reversal would have occurred.

Title Page

Abstract | Introduction

Conclusions | References

Tables | Figures

◄◄ | ►►

◄ | ►

Back | Close

Full Screen / Esc

Printer-friendly Version

Interactive Discussion

In Fig. 8c we show the difference in barotropic streamfunction $\Delta\Psi_B$ with respect to the reference configuration for the Miocene. The biggest changes in the flow occur in the Southern Ocean between South America and Africa. Also clearly visible is the change in the strength of the ACC, and a change in the strength of the equatorial current across the Atlantic through Panama Strait. To predict the change in $\Delta\Phi_P$ we can no longer use Eq. (16) since geometry changes lead to changes in δ and δ_τ as well. For the geometry in the reference configuration of the Miocene a value $\delta_{\tau,0} = 1.4\,\text{Sv}$ was computed in von der Heydt and Dijkstra (2005). The value of δ_τ in other geometries is then given by

$$\delta_\tau = \frac{f_{SA} - f_S}{f_{SA,0} - f_S}\delta_{\tau,0}. \tag{17}$$

For each geometry the value of δ and δ_τ is computed and we then use Eq. (12) to determine the transport Φ_P. In Fig. 8d the actual and predicted change in transport $\Delta\Phi_P = \Phi_P - \Phi_{P,0}$, with respect to the reference geometry, is plotted. Here we see that the predicted change matches the actual change quite well. We note that the predicted transport change is mainly determined by changes in δ and Φ_D whereas the contribution of changes in δ_τ is no more than 0.15 Sv.

3.5 Forcing

In this section we investigate whether or not the feature of flow reversal is robust with respect to changes in the forcing. The most important forcing is the prescribed surface wind stress $\boldsymbol{\tau}_0$, but in Sect. 2.1 we also noted that the gradients in the density field act as a forcing on the momentum equations. To examine the sensitivity with respect to these two forcings we introduce the dimensionless (so-called homotopy) parameters λ_τ and λ_ρ. The strength of the wind stress field and density field are then controlled by λ_τ and λ_ρ according to

$$\boldsymbol{\tau} = \lambda_\tau \boldsymbol{\tau}_0 \tag{18}$$

$$\alpha = \lambda_\alpha \alpha_0 \tag{19}$$

$$\beta = \lambda_\beta \beta_0. \tag{20}$$

Hence values of $\lambda_\rho = 1$ and $\lambda_\tau = 1$ correspond to the forcing of the reference configuration whereas $\lambda_\rho = 0$ and $\lambda_\tau = 0$ correspond to no forcing at all. We compute equilibrium solutions for several values of λ_ρ and λ_τ to see if the feature of flow reversal remains present.

Contrary to the configurations in Sect. 3.3 and Sect. 3.4, here the dimension of the state vector is not affected by the value of the control parameter. Therefore we can now use an efficient continuation method. Given an equilibrium solution for a certain value of the control parameter, we can use this as an initial condition for the JFNK method when computing equilibria for a slightly perturbed value of the control parameter. This reduces the number of Newton steps that is needed to reach an equilibrium. In the sensitivity experiments below we typically needed three or four Newton iterations to reach an equilibrium whereas in the spin-ups in Sect. 2.2 seven iterations were needed on average.

To consider the effect of the forcing of the density field we started from the reference solutions of Sect. 2.2 and decreased λ_ρ from a value $\lambda_\rho = 1$ to $\lambda_\rho = 0$ in steps $\Delta\lambda = -0.05$. It appears that the transport Φ_P shows hardly any sensitivity with respect to λ_ρ. The maximum change in transport $\Delta\Phi_P$ is given by approximately 0.12 Sv and 0.26 Sv for the Oligocene and Miocene, respectively (Fig. 9a). These changes are so small that for all values of λ_ρ the transport Φ_P remains eastward in the Oligocene and westward in the Miocene. In Fig. 9c and d, we plot the difference in barotropic streamfunction with respect to the reference configuration for $\lambda_\rho = 0$ for both Oligocene and Miocene configuration, respectively. Here we see that changes to the flow are not only small in Panama Strait, but actually throughout the whole domain. The baroclinic component in the barotropic streamfunction Φ_B is relatively small.

Similarly, we consider the effect of the strength of the wind forcing. We used natural parameter continuation in λ_τ to compute steady states in the range $0.75 < \lambda_\tau < 1.25$

using a size of the continuation step $\Delta\lambda_\tau = 0.025$. In Fig. 9b we plot the results for the Miocene and Oligocene configurations. Note that for all values of λ_τ we have $\Phi_P > 0$ for the Miocene and $\Phi_P < 0$ for the Oligocene, indicating that the flow reversal in Panama Strait is robust with respect to the strength of the wind stress.

4 Summary and conclusions

We applied the methodology of Bernsen et al. (2009) to investigate the wind-driven ocean circulation in the Oligocene and Miocene epochs. Using the JFNK method we efficiently found the same equilibrium solutions as with a time stepping spin-up run. A speed-up up to a factor 4.5 is obtained, depending on the desired accuracy of the solution. The flow reversal in Panama Strait during the transition from Oligocene to Miocene that was found in earlier studies is also present in the reference configuration of Sect. 2.1 that was used.

   We considered changes in the idealized bottom topography. Putting a ridge in the Thetys Seaway in the Oligocene geometry causes the flow in Panama Strait to reverse, provided that the ridge is high enough. A complete closing of the Thetys Seaway is not necessary for the flow to reverse. The linear equation Eq. (16), based on the physical mechanism proposed in Omta and Dijkstra (2003), predicts the changes in transport through Panama Strait extremely well. By putting a ridge in Drake Passage the strength of the ACC is reduced. According to the physical mechanism in Omta and Dijkstra (2003) this should lead to an increase in westward transport in Panama Strait and this is indeed what we find in the model. The linear equation Eq. (16), however, does not a very good job at predicting the change in flow through Panama Strait for this case. This can be attributed to the fact that friction and inertial terms can not be neglected in the ACC region.

   Further we considered changes in the continental geometry of Africa. In Omta and Dijkstra (2003) it was mentioned that the more southern location of Drake Passage, compared to South Africa, is essential for the flow reversal to occur. Indeed

Robustness of the Atlantic-Pacific flow reversal

E. Bernsen and
H. A. Dijkstra

Full Screen / Esc

we found that extending the geometry of South Africa to the latitudes of Drake Passage prevented the flow reversal in Panama Strait from occurring. The linear equation Eq. (12) can be used to predict the change in transport through Panama Strait very well, supporting the physical mechanism presented in Omta and Dijkstra (2003).

Further we looked at the sensitivity of the flow reversal with respect to wind forcing and buoyancy forcing, i.e. the forcing due to density differences. In the model we find that the ocean circulation shows only weak changes with respect to variations in the thermal expansion coefficient α_0 and saline contraction coefficient β_0. In particular the flow through Panama Strait changes no more than 0.26 Sv when the buoyancy forcing is entirely switched off. For the wind forcing we find a linear relation between the transport in Panama Strait and the amplitude of the wind stress field. In all cases we found that the feature of flow reversal during the transition from Oligocene to Miocene remains present in the model.

In summary, we conclude that the Atlantic-Pacific flow reversal between the Oligocene and the Miocene is a robust feature in MOM4. Whether it actually happened in the past, remains to be demonstrated from proxy data but we hope that this study will stimulate further research on this issue.

References

Barker, P. and Burrell, J.: The opening of Drake Passage, Mar. Geol., 25, 15–34, doi:10.1016/0025-3227(77)90045-7, 1977. 2484

Bernsen, E., Dijkstra, H. A., and Wubs, F. W.: Bifurcation analysis of wind-driven flows with MOM4, Ocean Model., 30, 95–105, doi:10.1016/j.ocemod.2009.06.003, 2009. 2486, 2489, 2490, 2492, 2495, 2501

Budd, A. F., Stemann, T. A., and Johnson, K. G.: Stratigraphic Distributions of Genera and Species of Neogene to Recent Caribbean Reef Corals, J. Paleontol., 68, 951–977, 1994. 2486

Dercourt, J., Gaetani, M., Vrielynck, B., Barrier, E., Biju-Duval, B., Brunet, M., Cadet, J., Crasquin, S., and Sandulescu, M.: Atlas Peri-Tethys, palaeogeographical maps, Commis-

sion de la Carte Géologique du Monde/Commission for the Geologic Map of the World, Paris, 2000. 2485, 2496

Edinger, E. N. and Risk, M. J.: Preferential Survivorship of Brooding Corals in a Regional Extinction, Paleobiology, 21, 200–219, 1995. 2486

5 Exon, N., Kennett, J., and Malone, M.: Shipboard Scientific Party, Leg 189 Summary, 2001. 2484

Godfrey, J. S.: A sverdrup model of the depth-integrated flow for the world ocean allowing for island circulations, Geophysical and Astrophysical Fluid Dynamics, 45, 89–112, 1989. 2485, 2493

10 Griffies, S., Harrison, M., Pacanowski, R., and Rosati, A.: A Technical Guide to MOM4, NOAA/Geophysical Fluid Dynamics Laboratory, available on-line at: http://www.gfdl.noaa.gov/fms, 2004. 2487

Hallam, A.: Faunal realms and facies in the Jurassic, Paleontology, 12, 1–18, 1969. 2484

Murray, R. J.: Explicit Generation of Orthogonal Grids for Ocean Models, J. Comput. Phys.,
15 126, 251–273, doi:10.1006/jcph.1996.0136, 1996. 2487

Nesbitt, H. W. and Young, G. M.: Sedimentation in the Venezuelan Basin, Circulation in the Caribbean Sea, and Onset of Northern Hemisphere Glaciation, J. Geol., 105, 531–544, 1997. 2486

Omta, A. W. and Dijkstra, H. A.: A physical mechanism for the Atlantic-Pacific flow reversal in
20 the early Miocene, Global Planet. Change, 36, 265–276, 2003. 2485, 2486, 2488, 2491, 2492, 2493, 2494, 2498, 2501, 2502

Ricou, L.: The Tethyan oceanic gates: a tectonic approach to major sedimentary changes within Tethys, Geodynamica Acta, 1, 225–232, 1987. 2485

Saad, Y.: Iterative Methods for Sparse Linear Systems, PWS Publishing Company, 1996. 2489
25 von der Heydt, A. and Dijkstra, H. A.: Flow reorganizations in the Panama Seaway: A cause for the demise of Miocene corals?, Geophys. Res. Lett., 32, L02609, doi:10.1029/2004GL020990, 2005. 2485, 2486, 2487, 2488, 2491, 2492, 2494, 2499, 2508

Title Page

Abstract | Introduction

Conclusions | References

Tables | Figures

|◄ | ►|

◄ | ►

Back | Close

Full Screen / Esc

Printer-friendly Version

Interactive Discussion

Table 1. Convergence history for the JFNK method applied to the Oligocene configuration. The norm of the residual is computed after the Newton step has been applied.

Newton iteration	Number of FGMRES iterations	Norm of residual
1	8	2.81×10^{-3}
2	79	1.18×10^{-3}
3	12	7.42×10^{-5}
4	25	1.13×10^{-6}
5	44	1.22×10^{-8}
6	46	1.08×10^{-10}
7	46	9.98×10^{-13}

Title Page

Abstract | Introduction

Conclusions | References

Tables | Figures

|◄ | ►|

◄ | ►

Back | Close

Full Screen / Esc

Printer-friendly Version

Interactive Discussion

Table 2. The CPU time used for the JFNK method and a time stepping run of 5 years.

	Oligocene	Miocene
N	210 618	208 014
Timestepper	5949 s	6088 s
JFNK	1317 s	1337 s
speed-up	4.5	4.6

Table 3. Volume transports (in Sverdrups) through Drake Passage (Φ_D), Panama Strait (Φ_P), the transport through a section from the tip of South Africa to Antarctica (Φ_{SA}), Thetys Seaway (Φ_T) and through the boundary of the North Atlantic and the arctic seas. Transports are given for the Miocene and Oligocene and a positive value indicates a transport into the Atlantic basin.

Transport	Oligocene	Miocene
Φ_P	−7.31 Sv	14.73 Sv
Φ_D	79.21 Sv	120.00 Sv
Φ_{SA}	−85.72 Sv	−134.46 Sv
Φ_T	13.82 Sv	2.46×10^{-4} Sv
Φ_A	5.64×10^{-4} Sv	−0.22 Sv
Φ_{tot}	-9.66×10^{-4} Sv	2.01×10^{-3} Sv

Table 4. Spherical coordinates of the points A and B that define the sections over which the transports through the Thetys Sea (Φ_T) and Drake Passage (Φ_D) are calculated in the Oligocene geometry.

Section	ϕ_A	θ_A	ϕ_B	θ_B
Φ_T	40° E	25° N	50° E	30° N
Φ_D	60° W	89° S	60° W	50° S
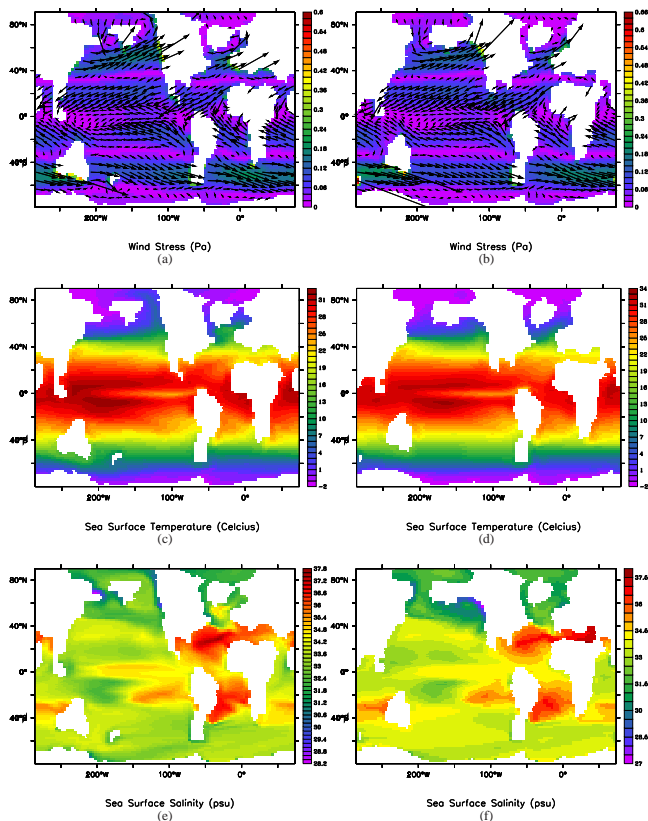
Fig. 1. The prescribed wind-stress field τ_0 in the **(a)** Oligocene and **(b)** Miocene configuration. The coloring indicates the strength $(\tau_{0,\phi}^2 + \tau_{0,\theta}^2)^{1/2}$ of the wind stress in Pa. **(c)** Sea surface temperature (°C) of the prescribed temperature field in the Oligocene configuration and **(d)** Miocene configuration. **(e)** Sea surface salinity (psu) of the prescribed salinity field in the Oligocene configuration and **(f)** Miocene configuration. All the fields are obtained as the time-average over the last 20 years of the spin-up CCSM1.4 simulations in von der Heydt and Dijkstra (2005).

2508
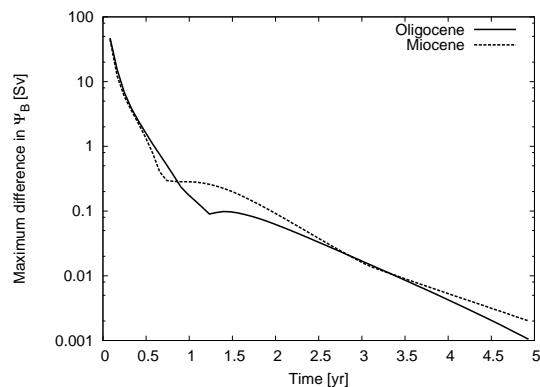
Fig. 2. The maximum difference in the barotropic streamfunction obtained using a timestepping spin-up run and JFNK as a function of the length of the spin-up run.
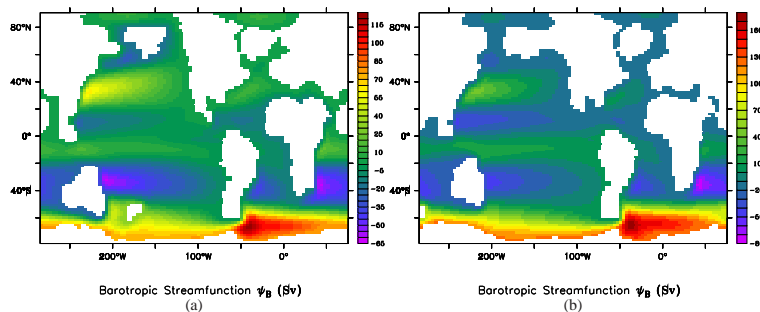
Fig. 3. The barotropic streamfunction (in Sverdrup) for the reference configuration for the Oligocene **(a)** and the Miocene **(b)** obtained using the JFNK method.
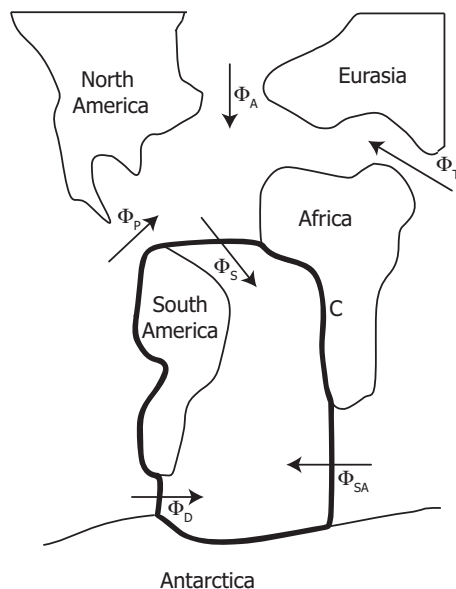
Fig. 4. Sketch of Atlantic Basin in the Oligocene Geometry. The thick line is the contour C over which the momentum equations are integrated to derive Eq. (4). The arrows denote the direction and location of the transports Φ_S, Φ_P, Φ_D, Φ_A, Φ_T and Φ_{SA}.

Robustness of the Atlantic-Pacific flow reversal

E. Bernsen and
H. A. Dijkstra
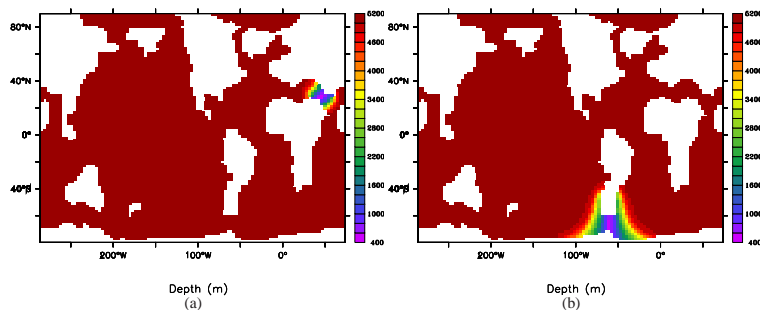
Fig. 5. The bathymetry for the Oligocene configuration with a ridge of maximum height $H = 4500$ m for **(a)** the Thetys Seaway and **(b)** Drake Passage. The coloring indicates the depth of the ocean in meters.
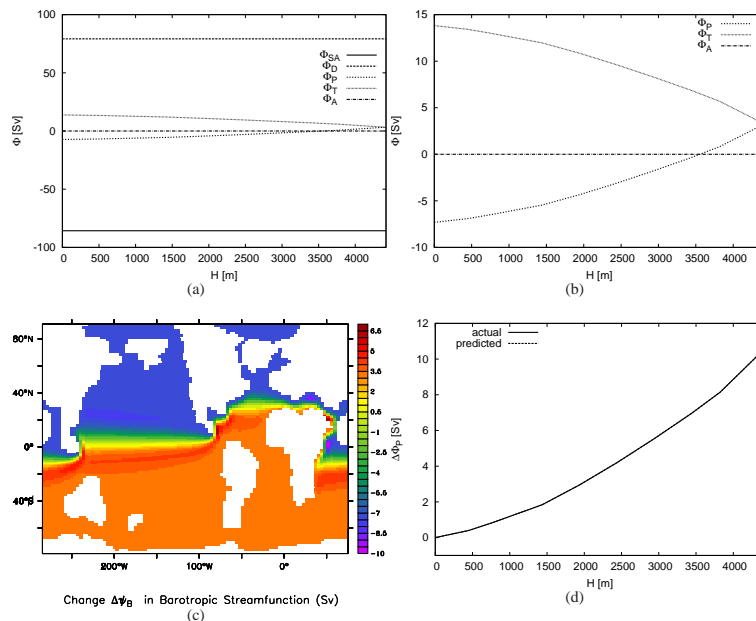
Fig. 6. (a) The transports Φ_P, Φ_A, Φ_T, Φ_{SA} and Φ_D in Sverdrup as a function of the height H of a ridge in the Thetys Seaway with a detailed view in **(b)**. **(c)** The difference $\Delta\Psi_B$ in barotropic streamfunction between the reference configuration for the Oligocene (flat bottom topography) and the configuration with the bottom topography depicted in Fig. 5a. **(d)** The actual and predicted change $\Delta\Phi_P$ in transport through Panama Strait computed using Eq. (16) as a function of the height H of a ridge in the Thetys Seaway. Note that the lines for actual transport and predicted transport overlap and are indistinguishable.
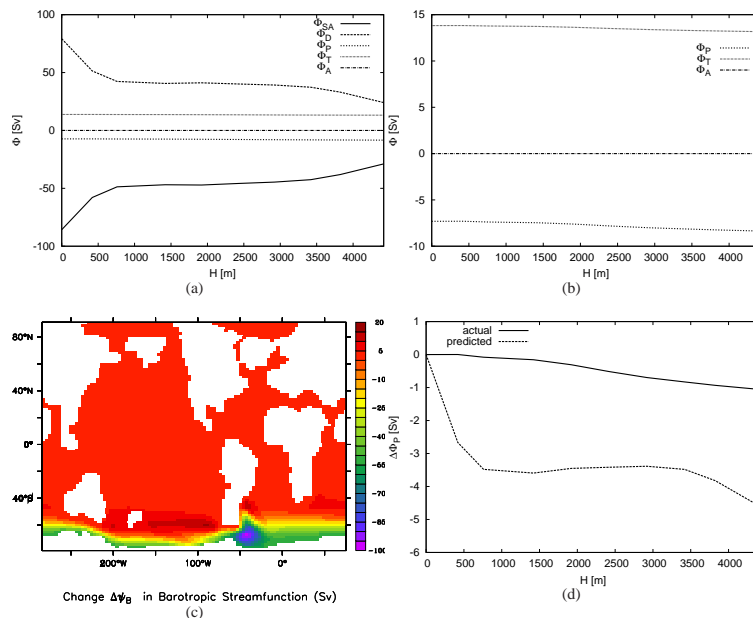
Fig. 7. (a) The transports Φ_P, Φ_A, Φ_T, Φ_{SA} and Φ_D in Sverdrup as a function of the height H of a ridge in the Drake Passage with a detailed view in **(b)**. **(c)** The difference $\Delta\Psi_B$ in barotropic streamfunction between the reference configuration for the Oligocene (flat bottom topography) and the configuration with the bottom topography depicted in 5b. **(d)** The actual and predicted change $\Delta\Phi_P$ in transport through Panama Strait computed using Eq. (16) as a function of the height H of a ridge in the Drake Passage.
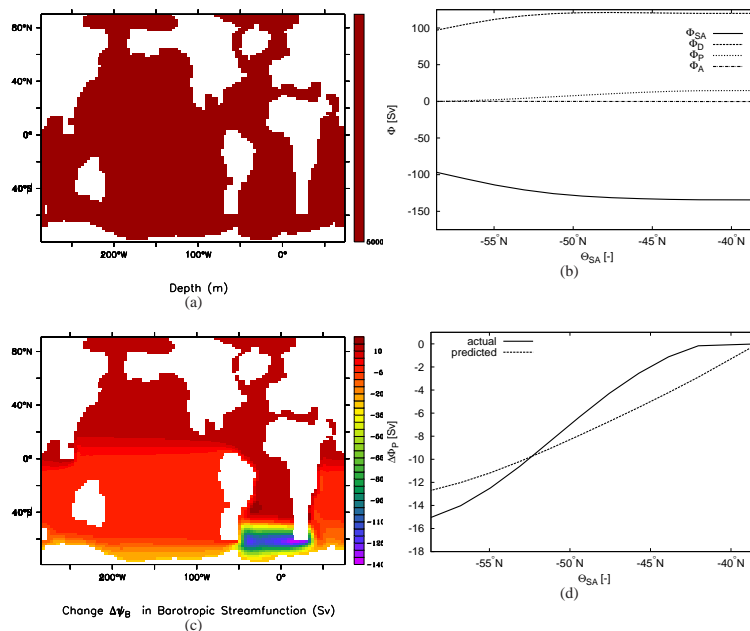
Fig. 8. (a) The geometry for the Miocene configuration with the tip of South Africa extended maximally southwards. Note that here we use a flat bottom topography. **(b)** The transports Φ_P, Φ_A, Φ_{SA} and Φ_D in Sverdrup as a function of the latitude of the tip of South Africa θ_{SA}. **(c)** The difference $\Delta\Psi_B$ in barotropic streamfunction between the reference configuration and the configuration with the geometry of **(a)**. **(d)** The actual and predicted change in transport $\Delta\Phi_P$ through Panama Strait as a function of the latitude of the tip of South Africa θ_{SA}.
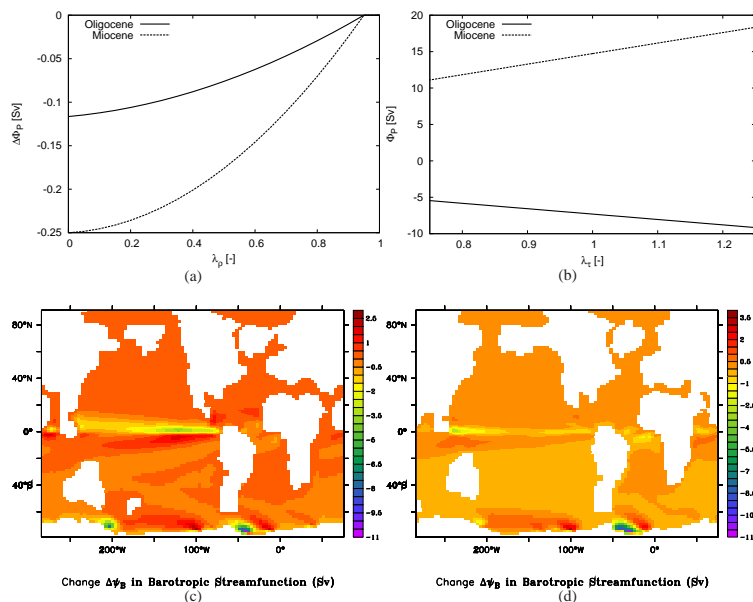
Fig. 9. The change $\Delta\Phi_P$ in transport through Panama Strait as a function of λ_ρ for the Oligocene and Miocene configuration. **(b)** The transport Φ_P through Panama Strait as a function of λ_τ. **(c–d)** Difference in barotropic streamfunction between reference configuration and configuration without buoyancy forcing ($\lambda_\rho = 0$) for the Oligocene **(c)** and Miocene **(d)**.